## Out-of-Time-Order Correlator Spectroscopy

Keisuke Fujii

Graduate School of Engineering Science, The University of Osaka,

1-3 Machikaneyama, Toyonaka, Osaka 560-8531, Japan

Center for Quantum Information and Quantum Biology,

The University of Osaka, 1-2 Machikaneyama, Osaka 560-0043, Japan and

RIKEN Center for Quantum Computing (RQC), Hirosawa 2-1, Wako, Saitama 351-0198, Japan

(Dated: December 1, 2025)

Out-of-time-order correlators (OTOCs) are central probes of quantum scrambling, and their generalizations have recently become key primitives for both benchmarking quantum advantage and learning the structure of Hamiltonians. Yet their behavior has lacked a unified algorithmic interpretation. We show that higher-order OTOCs naturally fit within the framework of quantum signal processing (QSP): each  $OTOC^{(k)}$  measures the 2k-th Fourier component of the phase distribution associated with the singular values of a spatially resolved truncated propagator. This explains the contrasting sensitivities of time-ordered correlators (TOCs) and higher-order OTOCs to causal-cone structure and to chaotic, integrable, or localized dynamics. Based on this understanding, we further generalize higher-order OTOCs by polynomial transformation of the singular values of the spatially resolved truncated propagator. The resultant signal allows us to construct frequency-selective filters, which we call OTOC spectroscopy. This extends conventional OTOCs into a mode-resolved tool for probing scrambling and spectral structure of quantum many-body dynamics.

#### I. INTRODUCTION

Quantum computers promise computational capabilities that surpass those of classical devices, enabling applications ranging from factorization [1], quantum simulation [2–4] and linear system solvers [5]. As hardware platforms continue to advance, a central challenge has emerged in determining how we can reliably characterize, benchmark, and ultimately understand the computational advantage of such quantum processors.

Early demonstrations, such as quantum computational supremacy experiments, have provided compelling evidence that quantum devices can generate output distributions intractable for classical supercomputers [6–9]. However, such sampling tasks face inherent limitations: their outputs are difficult to verify, highly susceptible to noise, and challenging to reproduce across heterogeneous quantum hardware. As devices grow in scale and fidelity, there is a strong need for benchmarking tools that remain both experimentally scalable and verifiable, while still probing highly complex patterns of quantum dynamics.

Out-of-time-order correlators (OTOCs) have emerged as physically grounded and experimentally accessible probes of the complexity of Hamiltonian dynamics [10–15]. Originally introduced in the context of quantum chaos and black-hole physics [10, 11, 13], OTOCs quantify the sensitivity of quantum evolution to perturbations and capture how local information spreads throughout a quantum system [12, 15]. Over the past decade, OTOCs have been measured in ultracold atoms [16], trapped ions [17–19], NMR systems [20, 21], and superconducting quantum processors [22, 23], revealing butterfly effects, operator spreading, and dynamical phase transitions.

Recent experimental advances have renewed and expanded the role of OTOCs in the characterization of

quantum dynamics. Google Quantum AI reported a generalized family of higher-order OTOCs implemented using nested echo circuits on a large-scale superconducting processor, observing order-resolved constructive interference at the edge of ergodicity [24]. Concurrently, an NMR-based experiment demonstrated precision OTOC measurements using coherent multi-pulse control sequences [25], showcasing once again the exceptional controllability of NMR, a platform that played a foundational role in the earliest demonstrations of quantum information processing.

Indeed, many core ideas in quantum control [26], dynamical decoupling [27, 28], and Hamiltonian engineering [29] were first developed in the context of NMR, and these techniques have had a profound and lasting influence on modern quantum algorithm design. A striking example of this intellectual lineage is the development of quantum signal processing (QSP) [30, 31] and its matrixvalued extension, the quantum singular value transformation (QSVT) [32, 33]. These frameworks, rooted in the physics of coherent control and phase-modulated pulse sequences, provide optimal means of implementing polynomial transformations of eigenvalues or singular values using only single-qubit rotations and controlled reflections. QSP and QSVT now underpin state-of-the-art quantum algorithms for Hamiltonian simulation [31] and linear systems [32].

Against this rich backdrop, a natural question arises: can the behavior of OTOCs be given a precise operational understanding through the lens of quantum algorithms? In this work, we show that the QSP framework provides exactly such an algorithmic perspective, yielding a clear and constructive operational understanding of higher-order OTOCs. We prove that higher-order OTOCs implemented via echo sequences correspond exactly to Chebyshev polynomial transformations of the

singular values of a spatially resolved truncated propagator  $A_{i,j}(t) = \langle 0_i | U(t) | 0_j \rangle$ . This perspective reveals that  $\mathrm{OTOC}^{(k)}$  directly measures the 2k-th Fourier component of the phase distribution associated with the singular values of  $A_{i,j}(t)$ . This is a clear answer to why time-ordered correlators (TOCs), i.e., the first harmonic often fail to detect causal-cone structures while higher-order OTOCs remain sharply sensitive to operator spreading and interference patterns.

We analyzed how the singular-value distributions and their associated phase distributions behave for several representative classes of dynamics including Haarrandom unitaries, dynamics outside the causal cone, and free-fermion evolution. These characteristic behaviors are further confirmed by numerical simulations, which demonstrate that higher-order OTOCs provide a sharp diagnostic of the arrival of the edge of ergodicity.

Building further on this connection, we introduce a generalized framework that we call OTOC spectroscopy. By replacing Pauli flips in the echo sequence with tunable Z-rotations, we obtain arbitrary degree-2d polynomial transformations of the singular values via depth-d QSP sequences. This enables frequency-selective filters, such as low-pass, high-pass, or band-pass, acting directly on the dynamical spectrum of the singular values of truncated propagator  $A_{i,j}(t)$ . Such filter-engineered OTOCs will allow us to isolate specific Fourier modes of the underlying phase distribution, providing a programmable and mode-resolved probe of scrambling, ergodicity, and spectral mixing in quantum many-body systems. This OTOC spectroscopy not only explains long-standing features of OTOC behavior across chaotic, integrable, and localized regimes, but also opens new avenues for designing scalable, verifiable, and spectrally-resolved diagnostics of complexity of quantum many-body dynamics.

### II. QSP FORMULATION OF OTOC $^{(k)}$

### A. Higher order OTOC

We consider an N-qubit system. Let U be an N-qubit unitary, such as a time-evolution operator  $U(t) = e^{-iHt}$ , for which we want to know the behavior of dynamics. We pick two sites i and j and define single-qubit Hermitian unitary (e.g. Pauli) operators  $B_i$  and  $M_j$  acting on the ith and jth qubits, respectively. The generalized OTOC echo operator is defined by [24]

$$C_{i,j} := U^{\dagger} B_i U M_j. \tag{1}$$

The kth-order OTOC between sites i and j is

$$OTOC_{i,j}^{(k)}(U, B_i, M_j) := \langle \psi_{ref} | C_{i,j}^{2k} | \psi_{ref} \rangle, \qquad (2)$$

for some reference state  $|\psi_{\rm ref}\rangle$ . In the following, we will focus on  $|0^N\rangle$  for concreteness. The exponent 2k arises naturally from the nested time-reversal structure of the echo sequence.

When k=1, this expression reduces to the usual commutator-squared OTOC under standard assumptions; higher k generalize the notion of operator spreading to multiple interference paths. For k=1/2 and  $B_i=M_i$ , the quantity  $\mathrm{OTOC}_{i,i}^{(1/2)}=\langle \psi_{\mathrm{ref}}|\,C_{i,i}\,|\psi_{\mathrm{ref}}\rangle$  corresponds to a conventional time-ordered correlator (TOC).

### B. QSP formulation

To connect this to a standard QSP setting with a single *probe* qubit, we introduce a SWAP gate  $S_{j\leftrightarrow i}$  that exchanges site j with a designated probe site i. We then define the modified unitary

$$\tilde{U} := US_{i \leftrightarrow i}. \tag{3}$$

In the Heisenberg picture, this simply relabels the site on which M acts, i.e.,  $M_i = S_{i \leftrightarrow i} M_i S_{i \leftrightarrow i}$ .

We now regard the *i*th (probe) qubit as an ancilla used for block encoding. Write  $\tilde{U}$  in block form with respect to the decomposition  $\mathcal{H} = \mathbb{C}^2 \otimes \mathcal{H}_{\text{sys}}$ :

$$\tilde{U} = \begin{pmatrix} A & B' \\ C' & D \end{pmatrix}, \qquad A = \langle 0_i | \tilde{U} | 0_i \rangle,$$

where A acts on the (N-1)-qubit system register. This is precisely a block-encoding of A. From the viewpoint of the original unitary U, the operator A is defined as

$$A_{i,j} = \langle 0_i | U | 0_j \rangle$$

such that the qubit indices of the truncation on the right and left sides differ. This distinction becomes important because it allows one to incorporate its spatial structure, such as the distance between i and j. Therefore we call  $A_{i,j}$  spatially resolved truncated propagator.

Let  $\lambda_l$  be the singular values of A, and let  $|\psi_l\rangle$  and  $|\phi_l\rangle$  denote the corresponding left and right singular vectors:

$$A |\phi_l\rangle = \lambda_l |\psi_l\rangle$$
.

By the qubitization [31, 32], the action of  $\tilde{U}$  on the 2-dimensional invariant subspace associated with each  $\lambda_l$  is given by a Y-basis rotation:

$$\tilde{U}_{\lambda_l} = e^{-i(\theta_l/2)Y}, \quad \cos(\theta_l/2) = \lambda_l.$$
 (4)

For definiteness, take B=M=Z acting on the probe qubit. Then

$$C = \tilde{U}^{\dagger} Z_i \tilde{U} Z_i,$$

and one finds that

$$C_{\lambda_l} = e^{i\theta_l Y}, \qquad C_{\lambda_l}^{2k} = e^{i2k\theta_l Y}.$$

Projection onto the probe state gives

$$\langle 0_i | \langle 0^{N-1} | C^{2k} | 0_i \rangle | 0^{N-1} \rangle = \sum_l |\alpha_l|^2 \cos(2k\theta_l) \qquad (5)$$

$$= \sum_{l} |\alpha_l|^2 T_{4k}(\lambda_l), \qquad (6)$$

where  $T_m$  is the Chebyshev polynomial of the first kind and  $|\psi_{\text{ref}}\rangle = |0^N\rangle = |0_i\rangle \otimes \sum_l \alpha_l |\psi_l\rangle$ . Specifically, for the reference state  $|0^N\rangle$ ,  $\alpha_l = \langle \psi_l | 0^{N-1} \rangle$ . Note that since we parametrize the singular values as  $\lambda = \cos(\theta/2)$ , the 2k-th harmonic  $\cos(2k\theta)$  corresponds to the 4k-th order Chebyshev polynomial  $\cos(2k\theta) = \cos(4k(\theta/2)) = T_{4k}(\lambda)$ .

**Theorem 1** (OTOC as a Chebyshev polynomial transform). Let U be the given dynamics and take  $B_i = Z_i$  and  $M_j = Z_j$  on the probe qubit. Then the kth-order OTOC associated with this echo sequence satisfies

$$OTOC^{(k)}(U, Z_i, Z_j) = \sum_{l} |\alpha_l|^2 \cos(2k\theta_l)$$
 (7)

$$= \sum_{l} |\alpha_l|^2 T_{4k}(\lambda_l), \qquad (8)$$

where  $\lambda_l$  are the singular values of  $A = \langle 0_i | \tilde{U} | 0_i \rangle$  with  $\tilde{U} = US_{j \leftrightarrow i}$  (or equivalently  $A_{i,j} = \langle 0_i | U | 0_j \rangle$ ) and  $|\psi_{\text{ref}}\rangle = |0_i\rangle \otimes \sum_l \alpha_l |\psi_l\rangle$ .

## III. BEHAVIOR OF $OTOC^{(k)}$ FROM THE VIEWPOINT OF FOURIER ANALYSIS

# A. Phase distribution of singular values of spatially resolved truncated propagator

From the above theorem, we see that the output of  $OTOC^{(k)}$  extracts a specific Fourier mode of the distribution function of the phase  $\theta$  corresponding to the singular values as follows. Let  $\lambda_l^{(i,j)}$  be the singular values and define the phase variables

$$\lambda_l^{(i,j)} = \cos(\theta_l^{(i,j)}/2), \qquad \theta_l^{(i,j)}(t) \in [0,\pi].$$

Then the distribution function of  $\theta$  can be given by

$$p_{i,j}(\theta) := \sum_{l} |\alpha_l^{(i,j)}|^2 \,\delta\Big(\theta - \theta_l^{(i,j)}\Big). \tag{9}$$

Now we realize

$$OTOC^{(k)}(U, Z_i, Z_j) = \int_0^{\pi} d\theta \cos(2k\theta) p_{i,j}(\theta).$$

 $OTOC^{(k)}$  corresponds to the 2k-th Fourier mode with  $cos(2k\theta)$ . Specifically, TOC with k = 1/2 corresponds to the first harmonic with  $cos(\theta)$ .

Although the phase distribution  $p_{i,j}(\theta)$  depends on the chosen reference state, the underlying distribution of  $\theta$  associated with the truncated unitary operator  $A_{i,j}$  is determined solely by the dynamics U and two sites i and j. In the following, we analyze how the behavior of this intrinsic phase distribution  $\tilde{p}_{i,j}(\theta)$  (or singular value distribution) of  $A_{i,j}$  governs the detectability of different Fourier modes (Chebyshev moments) and clarifies the contrasting responses of TOCs and higher-order OTOCs.

## B. Haar random unitary

When U is Haar random,  $\tilde{U} = US_{j\leftrightarrow i}$  is also Haar random. Then the spatially resolved truncated propagator

$$A_{i,j} = \langle 0_i | \tilde{U} | 0_i \rangle$$

is a truncated Haar unitary [34–36]. For such truncations, it is well known that the eigenvalues  $x = \lambda^2$  of  $A_{i,j}A_{i,j}^{\dagger}$  follow the Jacobi (or arcsine) ensemble with  $\alpha = \beta = -1/2$  in the limit of large N:

$$\rho_x(x) = \frac{1}{\pi\sqrt{x(1-x)}}, \qquad x \in (0,1), \tag{10}$$

where  $\lambda$  denotes the singular values of  $A_{i,j}$ .

Changing variables from  $x = \lambda^2$  to the singular value  $\lambda \in (0, 1)$  yields

$$\rho_{\lambda}(\lambda) = \rho(\lambda^2) \, 2\lambda = \frac{2}{\pi \sqrt{1 - \lambda^2}}, \qquad 0 < \lambda < 1. \tag{11}$$

Finally, using the phase parametrization

$$\lambda = \cos \frac{\theta}{2}, \qquad \theta \in (0, \pi),$$

the corresponding distribution of  $\theta$  becomes

$$\rho_{\theta}(\theta) = \rho_{\lambda}(\cos(\theta/2)) \left| \frac{d\lambda}{d\theta} \right| = \frac{1}{\pi}, \quad 0 < \theta < \pi. \quad (12)$$

Thus the intrinsic phase distribution of the truncated propagator is perfectly uniform on  $[0,\pi]$  in the Haarrandom limit.

As a consequence, all nontrivial Fourier components vanish:

$$\int_0^{\pi} \frac{1}{\pi} \cos(n\theta) d\theta = 0, \qquad n \ge 1,$$

and therefore both TOCs and higher-order OTOCs,  $OTOC^{(k)}$  decay to zero. This Haar-random distribution provides a natural reference against which nontrivial dynamical features, such as causal-cone edges, interference patterns, or localization, appear as deviations from the flat phase distribution and its Fourier harmonics.

#### C. Outside the causal-cone

To gain intuition for the opposite extreme, let us consider the case U=I. The truncated propagator reduces to

$$A_{i,j} = |0_j\rangle \otimes \langle 0_i| \otimes I_{m\neq i,j},$$

where  $I_{m\neq i,j}$  indicates the identity operator on the qubits except for *i*th and *j*th. As a result, the singular values of  $A_{i,j}$  take the exact bimodal form

$$\lambda \in \{0, 1\},$$
 with multiplicities  $2^{N-2}$  each,

corresponding respectively to non-propagating directions and projection-induced local directions.

Next, let us consider the case where ith site lies outside the causal cone of jth site. More precisely, we consider a short time scale  $t < d(i,j)/v_{LR}$  with d(i,j) being the distance between i and j, where the Lieb–Robinson bound ensures a correlation between i and j is not yet formed. The singular values of  $A_{i,j}(t)$  are the square roots of the eigenvalues of

$$C_{i,j}(t) := A_{i,j}(t)A_{i,j}(t)^{\dagger} = \langle 0_i | U(t)P_j U^{\dagger}(t) | 0_i \rangle, \quad (13)$$

where  $P_j := |0_j| \langle 0_j|$ . Thus the problem reduces to understanding the spectrum of the positive operator  $C_{i,j}(t)$ .

When ith and jth sites are outside of the causal cone, the Heisenberg-evolved projector

$$P_j(t) := U(t)P_jU^{\dagger}(t) \tag{14}$$

has support only on sites within a finite neighborhood of j, and in particular acts as the identity on site i. Equivalently,  $P_j(t)$  commutes with the local projector  $P_i := |0_i\rangle\langle 0_i|$ ,

$$[P_i, P_j(t)] \simeq 0$$
 for  $t < d(i, j)/v_{LR}$ , (15)

with  $v_{LR}$  being the Lieb–Robinson velocity. Hence  $C_{i,j}(t)$  is almost unitarily equivalent to  $C_{i,j}(0)$ , and its spectrum is almost identical to the spectrum in the trivial case U(t) = I.

The above discussion implies that even when the time t is small and j lies outside the causal-cone of i, the left and right truncations commute, resulting in the same bimodal distribution. Only when the causal-cone reaches the separation between i and j do the left and right truncations begin to communicate with overlap, after which the two-peak structure rapidly dissolves. In fully chaotic dynamics, the ensuing spectral mixing drives  $A_{i,j}(t)$  towards a truncated-Haar-like regime in which the phase distribution becomes nearly uniform, as will be corroborated by our numerical simulations.

## D. Algorithmic meanings of higher order OTOC

This dichotomy between a bimodal distribution (outside the causal cone) and a nearly uniform distribution (inside the cone under chaotic dynamics) has direct consequences for different Fourier modes. The TOC-like quantity corresponds to the first harmonic  $\cos \theta$ , but for a bimodal distribution supported at  $\theta = 0$  and  $\theta = \pi$ , we have

$$\cos 0 = +1, \qquad \cos \pi = -1,$$

so that the contributions cancel almost exactly. Thus, the first Fourier component of a bimodal distribution is nearly indistinguishable from that of the uniform (Haar) distribution, explaining why TOCs fail to detect the presence of a causal-cone edge.

In contrast, the second harmonic  $\cos(2\theta)$ , probed by OTOC<sup>(1)</sup> in our notation, takes the value +1 at both  $\theta = 0$  and  $\theta = \pi$ , whereas it averages to zero under a uniform distribution. Hence OTOC<sup>(1)</sup> is sharply sensitive to the appearance of a bimodal spectrum and provides a clear discriminator between non-propagating, projection-dominated behavior outside the causal cone and ergodic spectral mixing inside the cone.

Higher harmonics  $\cos(4\theta), \cos(6\theta), \ldots$ , corresponding to  $OTOC^{(k)}$  with  $k \geq 2$ , amplify this contrast even further, as their oscillatory structure selectively accentuates sharp peaks near the endpoints  $\theta = 0, \pi$ . Thus higher-order OTOCs act as progressively finer "spectral filters" that capture the detailed structure of the truncated propagator's phase distribution.

## E. Structural signature of underlying Hamiltonian

Next, let us examine how the phase distribution changes depending on the properties of the Hamiltonian. Suppose the dynamics U is given as a Hamiltonian evolution  $U = e^{-iHt}$  with respect to a Hamiltonian H. The truncated unitary is now defined depending on a time t:

$$A_{i,j}(t) = \langle 0_i | e^{-iHt} | 0_j \rangle.$$

The singular values of the truncated propagator  $A_{i,j}(t)$ quantify how strongly the time evolution transfers components of the input subspace conditioned on  $|0_i\rangle$  to the output subspace conditioned on  $\langle 0_i|$ . More precisely, if  $A_{i,j}(t) \left| \phi_l^{(j)} \right\rangle = \lambda_l(t) \left| \psi_l^{(i)} \right\rangle$  is the singular-value decomposition, then each  $\lambda_l(t) \in [0,1]$  measures the amplification (or more precisely attenuation since  $\lambda \leq 1$ ) with which the input direction  $\left|\phi_l^{(j)}\right\rangle$  is mapped into the output direction  $\left|\psi_l^{(i)}\right\rangle$ . When U is close to the identity or when i and j lie outside each other's causal cone, most input directions experience almost complete suppression, vielding  $\lambda_l(t) \simeq 0$ , while a few projection-induced local directions may satisfy  $\lambda_l(t) \simeq 1$ . Conversely, when coherent flow from j to i builds up, the largest singular values approach unity. Thus the singular-value distribution of  $A_{i,j}(t)$  directly encodes the structure and strength of information transfer between the two local subspaces.

A complementary viewpoint is obtained by inserting the spectral decomposition  $U(t) = \int e^{-i\omega t} E_H(d\omega)$ , where the operator-valued distribution function  $E_H(d\omega)$  is defined as follows:

$$E_H(d\omega) := \sum_a \delta(\omega - E_a) |E_a\rangle\langle E_a| d\omega.$$

This yields

$$A_{i,j}(t) = \int e^{-i\omega t} \langle 0_i | E_H(d\omega) | 0_j \rangle,$$

revealing that the truncated propagator is a coherent superposition of energy-resolved transfer channels between j and i. Different energy sectors  $\omega$  acquire phase factors  $e^{-i\omega t}$ , and their constructive or destructive interference, arising from energy differences  $\omega-\omega'$ , determines the growth, suppression, and temporal modulation of the singular values. Indeed, this can be understood explicitly by considering

$$A_{i,j}(t)A_{i,j}^{\dagger}(t)$$

$$= \iint e^{-it(\omega-\omega')} \langle 0_i | E_H(d\omega) | 0_j \rangle \langle 0_j | E_H(d\omega') | 0_i \rangle.$$

$$(17)$$

The eigenvalues of  $A_{i,j}(t)A^{\dagger}_{i,j}(t)$ , whose square roots correspond to the singular values of  $A_{i,j}(t)$ , are shaped by the interference kernel  $e^{-it(\omega-\omega')}$  coupling different energy sectors. When  $\omega \neq \omega'$ , rapid oscillations of this phase factor suppress off-diagonal contributions and drive the spectrum toward a mean-field, Haar-like form. On the other hand, when  $\omega$  and  $\omega'$  are aligned (e.g., due to integrability or localization), coherent reinforcement stabilizes sharp structures in the singular-value distribution.

## F. Free Fermion example

As an exercise, let us consider a free-fermionic Hamiltonian given by

$$H = \sum_{a,b} h_{ab} \hat{c}_a^{\dagger} \hat{c}_b, \tag{18}$$

where  $\hat{c}_a$  are fermionic annihilation operators and h is an  $N \times N$  single-particle hopping matrix. The many-body time evolution  $U(t) = e^{-iHt}$  is a Gaussian unitary, and the Heisenberg evolution of  $\hat{c}_a$  is governed by the single-particle propagator

$$U^{\dagger}(t)\hat{c}_{a}U(t) = \sum_{b} G_{ab}(t)\,\hat{c}_{b}, \qquad G(t) = e^{-iht}.$$
 (19)

The local projector  $P_j = |0_j\rangle\!\langle 0_j| = 1 - \hat{c}_j^\dagger \hat{c}_j$  evolves as

$$U(t)P_{j}U^{\dagger}(t) = 1 - \hat{c}_{j}^{\dagger}(t)\hat{c}_{j}(t), \qquad \hat{c}_{j}(t) = \sum_{a} G_{ja}(t)\hat{c}_{a}.$$
(20)

We now project site i onto  $|0_i\rangle$ . Writing

$$\hat{c}_j(t) = G_{ji}(t)\hat{c}_i + \sum_{a \neq i} G_{ja}(t)\hat{c}_a, \qquad (21)$$

and defining the vector v on the remaining modes by

$$v_a(t) := G_{ja}(t) \quad (a \neq i), \tag{22}$$

$$||v(t)||^2 = \sum_{a \neq i} |v_a(t)|^2 = 1 - |G_{ji}(t)|^2,$$
 (23)

we introduce a normalized fermionic mode

$$\hat{c}_v := \frac{1}{\|v\|} \sum_{a \neq i} v_a \, \hat{c}_a,\tag{24}$$

so that  $\hat{c}_j(t) = G_{ji}(t)\hat{c}_i + ||v(t)||\hat{c}_v$ . Substituting into  $U(t)P_jU^{\dagger}(t)$  and taking the expectation value in  $|0_i\rangle$ , all terms containing  $\hat{c}_i$  or  $\hat{c}_i^{\dagger}$  drop out, yielding

$$C_{i,j}(t) = \langle 0_i | U(t) P_j U^{\dagger}(t) | 0_i \rangle = 1 - ||v(t)||^2 \, \hat{c}_v^{\dagger} \hat{c}_v \quad (25)$$
$$= 1 - \left(1 - |G_{ij}(t)|^2\right) \hat{n}_v, \quad (26)$$

with  $\hat{n}_v := \hat{c}_v^{\dagger} \hat{c}_v$  the number operator for the single mode  $\hat{c}_v$ . Since  $\hat{n}_v$  has eigenvalues 0 and 1, the spectrum of

 $C_{i,j}(t)$  is

$$\lambda_0 = 1, \qquad \lambda_1 = |G_{ii}(t)|^2, \tag{27}$$

each with degeneracy  $2^{N-2}$  corresponding to the occupations of the other N-2 fermionic modes. Therefore, the singular values of the truncated propagator  $A_{i,j}(t)$  are 1 and  $|G_{ji}(t)|$ , where  $|G_{ji}(t)|^2$  is the single-particle propagation probability from j to i.

## G. Implications of Fourier mode analysis

On the other hand, in chaotic systems, the broad and irregular energy spectrum leads to rapid dephasing across sectors, driving the phase distribution  $p_{i,j}(\theta,t)$  toward a nearly uniform form characteristic of truncated Haar random matrices. In integrable systems, the quasiparticle structure of the spectrum induces persistent oscillatory patterns in  $\tilde{p}_{i,j}(\theta,t)$ , while in many-body localized systems the spectral weight remains concentrated near  $\theta \simeq 0$ , reflecting the stability of local integrals of motion. OTOCs provide a natural tool to probe these differences: TOC corresponds to the first Fourier mode, which nearly vanishes for both the bimodal distributions encountered outside the causal cone and the uniform distributions generated by chaotic mixing. In contrast, OTOC<sup>(1)</sup> and higher-order  $OTOC^{(k)}$  extract higher Fourier harmonics  $\cos(2k\theta)$  of  $\tilde{p}_{i,j}(\theta,t)$ , making them sharply sensitive to the presence of coherent peaks at  $\theta = 0, \pi$  as well as to finer interference structures arising from the underlying dynamics. This Fourier-mode viewpoint clarifies why higher-order OTOCs serve as powerful diagnostics of operator spreading and spectral mixing depending on the structure of given Hamiltonian. Chaotic, integrable, and many-body localized (MBL) dynamics produce distinct behaviors: chaotic dynamics lead to broad, nearly uniform distributions; integrable dynamics produce sharp, oscillatory features; and MBL dynamics yield distributions localized near  $\lambda \approx 1$  for i = j and rapidly decaying with |i-j|. These features will be verified with numerical simulations later.

## IV. OTOC SPECTROSCOPY VIA QSP

Building on the understanding that the QSP formulation of  $OTOC^{(k)}$  measures the 2k-th Fourier mode of the singular-value phase distribution, it is natural to generalize the construction by replacing the fixed Z flip in QSP with Z-rotations  $e^{-i\phi Z}$ . This introduces a transformation of the singular value of  $A_{i,j}$ , allowing us to form linear combinations of Fourier modes and thereby implement frequency-selective filter functions. As a natural extension of  $OTOC^{(k)}$ , we will refer to this framework as OTOC spectroscopy in the following.

To make this generalization explicit, we define singlequbit phase rotations on sites i and j as

$$B_i(\phi) := e^{-i\phi Z_i}, \qquad M_j(\phi) := e^{-i\phi Z_j}.$$

For each layer r = 1, ..., d, we introduce the generalized echo operator

$$C_{i,j}^{(r)}(t) := U^{\dagger}(t) B_i(\phi_{2r+1}) U(t) M_j(\phi_{2r}),$$
 (28)

where the phases  $\vec{\phi} = \{\phi_r\}$  are free parameters to be chosen according to the desired polynomial transformation.

Using these building blocks, we define the *d*-layer QSP-OTOC corresponding to a phase sequence  $\vec{\phi} = (\phi_0, \phi_1, \dots, \phi_{2d})$  as

QSP-OTOC<sub>i,j</sub><sup>(d)</sup>
$$(t, \vec{\phi}) := \langle 0^N | B_i(\phi_{2d}) \prod_{r=1}^d C_{i,j}^{(r)}(t) | 0^N \rangle.$$
(29)

For special choices of  $\vec{\phi}$ , this expression reduces to the standard higher-order OTOCs discussed above, where the action on each singular value  $\lambda = \cos(\theta/2)$  is given by the Chebyshev polynomial  $T_{4k}(\lambda)$  with k=d. In this sense, QSP-OTOC<sup>(d)</sup> provides a natural generalization of OTOC<sup>(k)</sup> in which the polynomial order and structure are controlled by the freely tunable phase sequence.

More generally, the sequence (29) implements, on each singular-value sector  $\lambda_l^{(i,j)}(t)$  of  $A_{i,j}(t)$ , a polynomial transformation

$$\lambda_l \mapsto P_{d,\vec{\phi}}(\lambda_l),$$

where  $P_{d,\vec{\phi}}(\lambda)$  is a degree-2d polynomial obtained through the standard QSP synthesis applied to the walk operator associated with  $A_{i,j}(t)$ . Thus,

$$\text{QSP-OTOC}_{i,j}^{(d)}(t, \vec{\phi}) = \sum_{l} |\alpha_{l}^{(i,j)}|^{2} P_{d, \vec{\phi}} \Big( \lambda_{l}^{(i,j)}(t) \Big) . \quad (30)$$

Since any real polynomial of degree at most 2d satisfying the standard QSP parity and boundedness constraints can be realized by an appropriate choice of phases  $\vec{\phi}$ , the QSP-OTOC implements a linear combination of Fourier harmonics of the phase distribution  $\tilde{p}_{i,j}(\theta,t)$  that lies

within the class of bounded degree-2d polynomials implementable by QSP. This enables the design of frequency-selective filters acting on the phase spectrum of  $A_{i,j}(t)$ . For instance, low-pass, high-pass, and band-pass filters can be designed to detect a characteristic feature of the Hamiltonian dynamics of interest. In chaotic or Haarrandom regimes, where  $p_{i,j}(\theta,t)$  approaches a nearly uniform distribution, such filters enable a refined diagnosis of residual structure and deviations from randomness. Conversely, in integrable or many-body localized dynamics, where  $p_{i,j}(\theta,t)$  exhibits sharp spectral support, QSP-OTOCs provide a powerful means to resolve the underlying interference structure by selectively probing specific harmonics of the phase distribution.

In summary, the freedom to engineer  $P_{d,\vec{\phi}}(\lambda)$  through QSP transforms the OTOC protocol into a fully programmable spectroscopic tool, which allows us to isolate dynamical features that are invisible to fixed-order OTOCs and greatly extending the versatility of out-of-time-order diagnostics.

#### V. NUMERICAL EXPERIMENTS

To substantiate the QSP-based interpretation developed above, we perform numerical simulations to see the singular value distributions of the truncated propagators  $A_{i,j}(t)$  and time-dependent behavior of their Fourier modes (for the corresponding phase distribution) under several physically relevant many-body Hamiltonians.

### A. Models

We consider three benchmark one-dimensional spin chains:

Chaotic (ergodic) model: a XYZ chain with a magnetic field [37]

$$H_{\rm chaos} = \sum_{i} (J_{x} X_{i} X_{i+1} + J_{y} Y_{i} Y_{i+1} + J_{z} Z_{i} Z_{i+1}) + h \sum_{i} Z_{i},$$

where we specifically choose  $J_x = -0.4$ ,  $J_y = -2.0$ ,  $J_z = -1.0$  and h = 0.75.

Integrable model: an XXZ chain with uniform field

$$H_{\text{int}} = \sum_{i} J(X_i X_{i+1} + Y_i Y_{i+1} + \Delta Z_i Z_{i+1}) + h \sum_{i} Z_i,$$

where we take  $J=1, \Delta=0$ , and h=0 as a free-fermion case. We also consider J=1, anisotropy  $\Delta=1$ , and a uniform field h=0.2, which yields an interacting integrable model solvable by the Bethe ansatz.

MBL model: a strongly disordered Heisenberg chain

$$H_{\text{MBL}} = \sum_{i} J(X_i X_{i+1} + Y_i Y_{i+1} + Z_i Z_{i+1}) + \sum_{i} h_i Z_i,$$

where J=1 and the on-site fields  $h_i$  are drawn uniformly at random from the interval [-h, h] with h=5, ensuring  $|h_i| \gg J$  and hence localization.

System sizes N=10 are diagonalized exactly. Time evolution is computed via  $U(t)=e^{-iHt}$  using standard exponentiation routines. For any pair of sites i,j, the truncated propagator is extracted as

$$A_{i,j}(t) = \langle 0_i | U(t) | 0_j \rangle$$
.

This operator is of dimension  $2^{N-1}\times 2^{N-1}$  and its singular values  $\lambda_l^{(i,j)}(t)$  are obtained via singular value decomposition.

We study the time evolution of the intrinsic phase distributions of the singular values:

$$\tilde{p}_{i,j}(\theta,t) = \frac{1}{D} \sum_{l} \delta(\theta - \theta_l^{(i,j)}(t)), \tag{31}$$

with D being the dimension, where  $\theta_l^{(i,j)}(t) = 2\arccos(\lambda_l^{(i,j)}(t))$ . Furthermore, we also observe kth order Chebyshev mode of the distribution of the singular values  $\lambda_l^{(i,j)}(t)$ :

$$\mathcal{M}_{4k}^{(i,j)}(t) = \frac{1}{D} \sum_{l} T_{4k} \left( \lambda_l^{(i,j)}(t) \right),$$

for 4k = 2, 4, 8, 12, each of which corresponds to TOC, OTOC<sup>(1)</sup>, OTOC<sup>(2)</sup> and OTOC<sup>(3)</sup>, respectively.

#### B. Results

Figure 1 illustrates the full time evolution of the phase distribution  $\tilde{p}_{i,j}(\theta,t)$  associated with the singular values of the spatially resolved truncated propagator  $A_{i,j}(t)$  for chaotic, integrable, and MBL dynamics, with i=0 and j=9. The four panels correspond, from top left to bottom right, to the chaotic, integrable (Bethe ansatz), integrable (free-fermion), and MBL chains, respectively, providing a direct visualization of the causal structure and the qualitative nature of the underlying many-body dynamics.

At the initial time t=0, when U(t)=I, the truncated propagator  $A_{i,j}(0)=\langle 0_i|\,I\,|0_j\rangle$  exhibits an exactly bimodal singular-value spectrum: all weight is concentrated at  $\theta=0$  and  $\theta=\pi$ , corresponding respectively to the local projection channel and the completely suppressed nonlocal channel. This yields a phase distribution  $\hat{p}_{i,j}(\theta,0)$  with two sharp peaks at the endpoints of the interval  $[0,\pi]$ .

As time evolves, the behavior of the phase distribution changes dramatically once the influence of site j reaches site i. In both the chaotic and integrable (Bethe ansatz) chains, once site i=0 enters the causal cone of site j=9 between t=1 and t=2, the initial bimodal structure collapses. Beyond this point, the subsequent evolution

reflects the qualitative nature of the underlying dynamics. In the chaotic chain, the distribution quickly relaxes toward a broad, nearly featureless profile approaching the truncated-Haar limit, with no residual oscillation in  $\theta$ . In contrast, the integrable (Bethe ansatz) chain displays pronounced and persistent oscillatory patterns: spectral weight flows coherently across  $\theta$ , producing the characteristic interference fringes associated with stable quasiparticle modes. This is more evident for the integrable (free-fermion) chain, where the initial peak at  $\theta=\pi$  begins to oscillate once the causal cone reaches the site j=9. This behavior is completely consistent with the analytical argument given for the free-fermion case above.

The behavior in the MBL chain is strikingly different. Because localization prevents ballistic propagation, site i remains effectively outside the causal cone of site j for all accessible times. As a result, the phase distribution retains its initial bimodal form, with weight pinned near  $\theta \simeq 0$  and  $\theta \simeq \pi$  and no evidence of the spectral mixing seen in the chaotic and integrable cases.

These observations demonstrate that the complexity of the dynamics — ergodic, integrable (free-fermion, Bethe ansatz), or localized — is vividly encoded in the singular-value statistics of the spatially resolved truncated propagator. The phase distribution  $\tilde{p}_{i,j}(\theta,t)$  provides a direct, mode-resolved signature of information spreading and clearly delineates the qualitative differences between chaotic mixing, coherent quasiparticle propagation, and localization-protected dynamics.

Figure 2 displays the time evolution of the Chebyshev moments  $\langle T_{4k}(\lambda) \rangle$  of the singular-value distribution of the truncated propagator  $A_{i,j}(t)$  under the chaotic Hamiltonian, for k=1/2 (TOC), k=1 (OTOC<sup>(1)</sup>), k=2 (OTOC<sup>(2)</sup>), and k=3 (OTOC<sup>(3)</sup>). Each curve corresponds to a different separation j, allowing us to track how the spatially resolved moments change as site i enters the causal cone of site j.

In the leftmost panel (k=1/2), the curve for j=0 reproduces the standard TOC, which decays monotonically from its initial value of 1. For  $j\neq 0$ , however, the spatially resolved TOC does not clearly detect the arrival of the causal-cone edge. As explained earlier, the second-order Chebyshev moment  $T_2(\lambda)$  corresponds to the first Fourier harmonic  $\cos\theta$ , which takes opposite signs at  $\theta=0$  and  $\theta=\pi$ . Consequently, a bimodal distribution and a nearly uniform distribution yield similar averaged signals, making the TOC largely insensitive to whether (i,j) lies inside or outside the causal cone. Indeed, for all  $j\neq 0$ , the TOC signal rises from zero and settles to a small value (approaching 0 in the Haar-random limit), without a sharp signature of the causal-cone crossing.

In the second panel (k = 1), the moment corresponds to the second Fourier harmonic  $\cos(2\theta)$ , i.e., the fourthorder Chebyshev polynomial  $T_4$ . Although  $\cos(2\theta)$  takes the value +1 at  $\theta = 0$  and  $\theta = \pi$ , it has relatively broad support there. As a result, when the initially bimodal phase distribution begins to deform at early

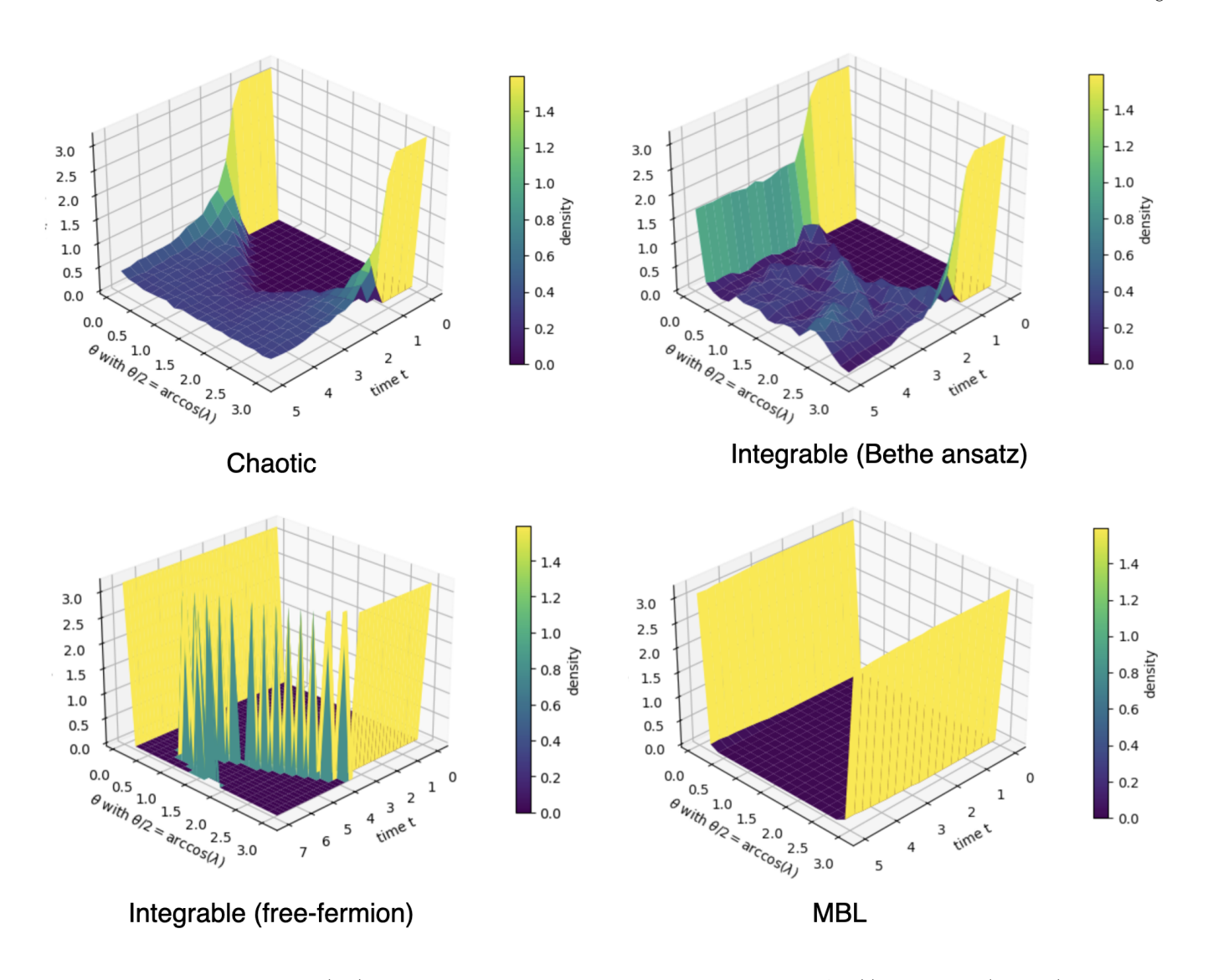


FIG. 1. Phase distributions  $\tilde{p}_{0,9}(\theta,t)$  of the singular values of the truncated propagator  $A_{0,9}(t)$  for chaotic (left top), integrable (Bethe ansatz) (right top), integrable (free-fermion) (left bottom) and MBL (right bottom) dynamics. The horizontal axes show time t ( $0 \le t \le 7$  for integrable (free-fermion) and  $0 \le t \le 5$  for others) and the phase variable  $\theta$  with  $\lambda = \cos(\theta/2)$ , and the vertical axis and color scale indicate the density.

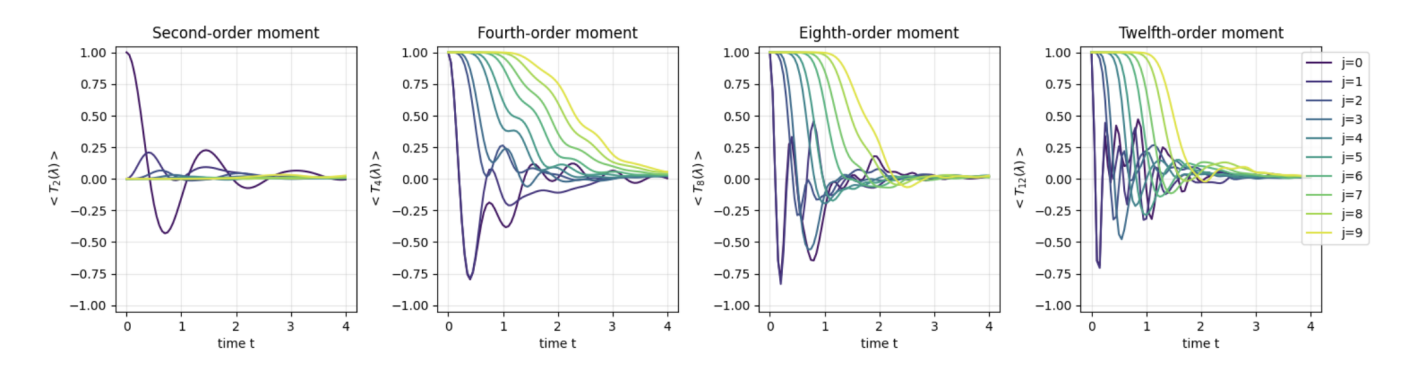


FIG. 2. Time evolution of the second-, fourth-, eighth-order, and twelfth-order Chebyshev moments  $\langle T_{4k}(\lambda) \rangle$  of the truncated propagator  $A_{i,j}(t)$  for the chaotic Hamiltonian, corresponding respectively to the TOC (k=1/2), OTOC<sup>(1)</sup> (k=1), OTOC<sup>(2)</sup> (k=2), and OTOC<sup>(3)</sup> (k=3) from left to right. Each curve shows the moment for a different separation j=0,...,9 where i=0.

times—before becoming completely flat—the averaged value of  $\cos(2\theta)$  decays only gradually. Thus the resulting OTOC<sup>(1)</sup> does not sharply detect the causal-cone arrival.

A sharp distinction first emerges for k=2 (third panel), corresponding to  $\cos(4\theta)$  and the eighth-order Chebyshev polynomial  $T_8$ . The higher harmonic strongly amplifies narrow peaks near  $\theta=0$  and  $\theta=\pi$ , making the averaged signal highly sensitive to even small departures from a bimodal distribution. Consequently, the moment exhibits a sharp and rapid decay when the causal cone reaches site j, cleanly resolving the light-cone structure and giving a clear spectral signature of operator spreading.

Finally, for k=3 (rightmost panel), corresponding to  $\cos(6\theta)$  and the twelfth-order Chebyshev polynomial  $T_{12}$ , the behavior becomes even sharper. The sixth harmonic further narrows the effective support around  $\theta=0$  and  $\theta=\pi$ , dramatically enhancing sensitivity to fine structure in the phase distribution. Thus  $OTOC^{(3)}$  shows an even more pronounced, nearly discontinuous drop at the causal-cone arrival time.

Taken together, these numerical observations are fully consistent with the theoretical picture developed in this work: TOCs probe only the first Fourier mode and thus fail to resolve the transition from bimodal to mixed phase distributions, whereas higher-order  ${\rm OTOC}^{(k)}$  extract higher harmonics that sharply reveal the onset of scrambling and the structure of the causal cone. These results substantiate our claim that  ${\rm OTOC}^{(k)}$  and QSP-based OTOC spectroscopy provide mode-resolved diagnostics of many-body dynamics that go well beyond conventional OTOC measurements.

## VI. CONCLUSION AND DISCUSSION

We have demonstrated that OTOCs admit a natural and powerful reformulation within the framework of

quantum signal processing. Higher-order OTOCs correspond to Chebyshev polynomial transformations of the singular values of spatially resolved truncated propagators  $A_{i,j}(t)$ . In the fully chaotic (Haar random) limit, the singular values follow an arcsine law and all nontrivial Fourier components of the eigenphase distribution vanish, explaining the decay of  $OTOC^{(k)}$ .

For Hamiltonian dynamics, however, the singular-value distributions or corresponding phase distributions retain rich structure reflecting locality, causal-cone propagation, and integrability or localization. We have shown that TOCs probe only first moments of self blocks  $A_{i,i}(t)$  and therefore lose dynamical information rapidly, whereas OTOC and more general QSP-OTOCs probe higher Chebyshev moments of two-point blocks  $A_{i,j}(t)$  and thus remain sensitive to operator spreading and coherent interference patterns deep into the scrambling regime.

By generalizing Pauli operations to tunable rotations, QSP-OTOCs implement arbitrary polynomial filters on the singular spectrum of  $A_{i,j}(t)$ . This enables new forms of "OTOC spectroscopy," in which slow modes, fast modes, and intermediate interference structures can be selectively amplified by appropriate choices of  $P(\lambda)$ . We expect this perspective to be useful not only for interpreting current quantum echo experiments, but also for designing new protocols that probe many-body dynamics in a mode-resolved fashion with full spatial resolution.

## ACKNOWLEDGMENTS

KF would like to thank Kaoru Mizuta and Tatsuhiko N. Ikeda for valuable and insightful discussions. This work is supported by MEXT Q-LEAP Grant No. JP-MXS0120319794, JST CREST JPMJCR24I3, and JST COI-NEXT No. JPMJPF2014.

- [1] P. W. Shor, in *Proceedings 35th annual symposium on foundations of computer science* (Ieee, 1994) pp. 124–134.
- [2] S. Lloyd, Science **273**, 1073 (1996).
- [3] D. S. Abrams and S. Lloyd, Physical Review Letters 83, 5162 (1999).
- [4] A. Aspuru-Guzik, A. D. Dutoi, P. J. Love, and M. Head-Gordon, Science 309, 1704 (2005).
- [5] A. W. Harrow, A. Hassidim, and S. Lloyd, Physical review letters 103, 150502 (2009).
- [6] F. Arute, K. Arya, R. Babbush, D. Bacon, J. C. Bardin, R. Barends, R. Biswas, S. Boixo, F. G. Brandao, D. A. Buell, et al., Nature 574, 505 (2019).
- [7] Y. Wu, W.-S. Bao, S. Cao, F. Chen, M.-C. Chen, X. Chen, T.-H. Chung, H. Deng, Y. Du, D. Fan, et al., Physical review letters 127, 180501 (2021).
- [8] A. Morvan, B. Villalonga, X. Mi, S. Mandra, A. Bengtsson, P. Klimov, Z. Chen, S. Hong, C. Erickson, I. Droz-

- dov, et al., arXiv preprint arXiv:2304.11119 (2023).
- [9] M. DeCross, R. Haghshenas, M. Liu, E. Rinaldi, J. Gray, Y. Alexeev, C. H. Baldwin, J. P. Bartolotta, M. Bohn, E. Chertkov, et al., arXiv preprint arXiv:2406.02501 (2024).
- [10] A. I. Larkin and Y. N. Ovchinnikov, Sov Phys JETP 28, 1200 (1969).
- [11] S. H. Shenker and D. Stanford, Journal of High Energy Physics 2014, 1 (2014).
- [12] P. Hosur, X.-L. Qi, D. A. Roberts, and B. Yoshida, Journal of High Energy Physics 2016, 1 (2016).
- [13] J. Maldacena, S. H. Shenker, and D. Stanford, Journal of High Energy Physics 2016, 1 (2016).
- [14] B. Swingle, G. Bentsen, M. Schleier-Smith, and P. Hayden, Physical Review A 94, 040302 (2016).
- [15] D. A. Roberts and B. Yoshida, Journal of High Energy Physics 2017, 1 (2017).
- [16] S. Pegahan, I. Arakelyan, and J. Thomas, Physical Re-

- view Letters 126, 070601 (2021).
- [17] M. Gärttner, J. G. Bohnet, A. Safavi-Naini, M. L. Wall, J. J. Bollinger, and A. M. Rey, Nature Physics 13, 781 (2017).
- [18] K. A. Landsman, C. Figgatt, T. Schuster, N. M. Linke, B. Yoshida, N. Y. Yao, and C. Monroe, Nature 567, 61 (2019).
- [19] M. K. Joshi, A. Elben, B. Vermersch, T. Brydges, C. Maier, P. Zoller, R. Blatt, and C. F. Roos, Physical Review Letters 124, 240505 (2020).
- [20] J. Li, R. Fan, H. Wang, B. Ye, B. Zeng, H. Zhai, X. Peng, and J. Du, Physical Review X 7, 031011 (2017).
- [21] K. X. Wei, C. Ramanathan, and P. Cappellaro, Physical review letters 120, 070501 (2018).
- [22] A. M. Green, A. Elben, C. H. Alderete, L. K. Joshi, N. H. Nguyen, T. V. Zache, Y. Zhu, B. Sundar, and N. M. Linke, Physical Review Letters 128, 140601 (2022).
- [23] J. Braumüller, A. H. Karamlou, Y. Yanay, B. Kannan, D. Kim, M. Kjaergaard, A. Melville, B. M. Niedzielski, Y. Sung, A. Vepsäläinen, et al., Nature Physics 18, 172 (2022).
- [24] Nature **646**, 825 (2025).
- [25] C. Zhang, R. Cortiñas, A. Karamlou, N. Noll, J. Provazza, J. Bausch, S. Shirobokov, A. White, M. Classen, S. Kang, et al., arXiv preprint

- arXiv:2510.19550 (2025).
- [26] U. Haeberlen, High Resolution NMR in solids selective averaging: supplement 1 advances in magnetic resonance, Vol. 1 (Elsevier, 2012).
- [27] L. Viola and S. Lloyd, Physical Review A 58, 2733 (1998).
- [28] G. S. Uhrig, PHYSICAL REVIEW LETTERS 106 (2011).
- [29] J. S. Waugh, L. M. Huber, and U. Haeberlen, Physical Review Letters 20, 180 (1968).
- [30] G. H. Low and I. L. Chuang, Physical review letters 118, 010501 (2017).
- [31] G. H. Low and I. L. Chuang, Quantum 3, 163 (2019).
- [32] A. Gilyén, Y. Su, G. H. Low, and N. Wiebe, in Proceedings of the 51st annual ACM SIGACT symposium on theory of computing (2019) pp. 193–204.
- [33] J. M. Martyn, Z. M. Rossi, A. K. Tan, and I. L. Chuang, PRX quantum 2, 040203 (2021).
- [34] K. Zyczkowski and H.-J. Sommers, Journal of Physics A: Mathematical and General 33, 2045 (2000).
- [35] B. Collins, Probability theory and related fields 133, 315 (2005).
- [36] Z. Dong, T. Jiang, and D. Li, Journal of Mathematical Physics 53 (2012).
- [37] N. Shiraishi, Europhysics Letters **128**, 17002 (2019).